nature structural & molecular biology

Solution structure of discoidal high-density lipoprotein particles with a shortened apolipoprotein A-I

Stefan Bibow[1], Yevhen Polyhach[1], Cédric Eichmann[1], Celestine N Chi[1], Julia Kowal[2], Stefan Albiez[2], Robert A McLeod[2], Henning Stahlberg[2], Gunnar Jeschke[1], Peter Güntert[1,3] & Roland Riek[1]

High-density lipoprotein (HDL) particles are cholesterol and lipid transport containers. Mature HDL particles destined for the liver develop through the formation of intermediate discoidal HDL particles, which are the primary acceptors for cholesterol. Here we present the three-dimensional structure of reconstituted discoidal HDL (rdHDL) particles, using a shortened construct of human apolipoprotein A-I, determined from a combination of nuclear magnetic resonance (NMR), electron paramagnetic resonance (EPR) and transmission electron microscopy (TEM) data. The rdHDL particles feature a protein double belt surrounding a lipid bilayer patch in an antiparallel fashion. The integrity of this structure is maintained by up to 28 salt bridges and a zipper-like pattern of cation-π interactions between helices 4 and 6. To accommodate a hydrophobic interior, a gross 'right-to-right' rotation of the helices after lipidation is necessary. The structure reflects the complexity required for a shuttling container to hold a fluid lipid or cholesterol interior at a protein:lipid ratio of 1:50.

HDL particles are transport containers in the circulatory system that receive cellular cholesterol and lipids destined for the liver and other lipoprotein particles. The metabolism of HDL particles is a complex process in which proteins, receptors and enzymes function in a coordinated manner to transport lipids and cholesterol between cells, tissues, organs and other lipoproteins[1]. Because low levels of HDL cholesterol often indicate an increased risk for cardiovascular diseases, HDL particles are also considered as important pharmacological targets for therapeutic strategies[2–4]. The 243-residue-long apolipoprotein A-I (apoA-I) is the major protein component in HDL particles[5]. Whereas residues 1–43 are postulated to prefer protein-protein interactions[6], the proximate ten tandem 11- or 22-residue repeats are proposed to represent the lipid-binding region, defining the diameter of the discoidal HDL particle[6–10]. Maturation into spherical HDLs is a two-step process. First, cholesterol and other lipids are incorporated into lipid-free apoA-I by ATP-binding cassette transporter A1 (ABCA1) via unknown mechanisms to form discoidal HDLs that contain two copies of apoA-I[11]. Second, binding to apoA-I and esterification of cholesterol by the enzyme lecithin/cholesterol acyltransferase (LCAT) transforms discoidal HDLs into mature spherical HDLs[1,12–14]. The transfer of cholesteryl ester and lipids between lipoprotein particles, however, is mediated by cholesteryl ester transfer protein (CETP), which also seems to rely on a direct interaction with apoA-I[15,16]. Therefore, apoA-I serves not only as a scaffold for shuttling lipids and cholesterol in a hydrophilic environment, but also as a binding hub facilitating maturation and interparticle communication. Notably, the structural organization of reconstituted and plasma-derived HDL particles is similar[11,17]. Whereas a flattened structure for each of the two apoA-I molecules is proposed for discoidal HDL particles, bending of apoA-I of 60° or more with inflection points at helices 5 and 10 is proposed for spherical HDL particles[11,17].

Although discoidal HDL particles are of high biophysical and medical importance[2,4,18–20], heterogeneity in their density, size, shape, and protein and lipid composition, as well as their large size of ~160 kDa (ref. 18), has prohibited detailed molecular and structural description with standard techniques such as X-ray crystallography and solution-state NMR spectroscopy[5]. Here we present the three-dimensional (3D) solution structure of rdHDLs assembled from MSPΔH5, a shortened version of apoA-I lacking the non-lipid-binding residues 1–54 (refs. 6,10) and 121–142 (proposed to form helix 5)[18], and the lipid 1,2-dimyristoyl-*sn*-glycero-3-phosphocholine (DMPC). Furthermore, we show by chemical shift comparison and lipid paramagnetic relaxation enhancement experiments that rdHDLs with and without helix 5 are structurally similar (**Supplementary Fig. 1**).

RESULTS

NMR spectroscopy assignment and secondary structure of rdHDL

rdHDLs assembled from MSPΔH5 and the lipid DMPC via an established procedure (Online Methods)[18,19] behaved well as determined by size-exclusion chromatography and blue native PAGE (**Supplementary Fig. 1f**), possessed the typical discoidal form as shown by negative-stain TEM (**Fig. 1** and **Supplementary Fig. 2**) and showed high-quality 2D [^{15}N,^{1}H]-TROSY spectra. However, initial attempts toward complete sequential assignment of uniformly labeled ^{2}H,^{13}C, ^{15}N-MSPΔH5 rdHDLs by TROSY-HNCA (tr-HNCA), tr-HN(CO)CA, tr-HNCACB[21] and [^{1}H,^{1}H]-NOESY-[^{15}N,^{1}H]-HMQC failed.

[1]Laboratory of Physical Chemistry, ETH Zurich, Zurich, Switzerland. [2]Center for Cellular Imaging and NanoAnalytics, Biozentrum University of Basel, Basel, Switzerland. [3]Institute of Biophysical Chemistry, Goethe-University Frankfurt am Main, Frankfurt am Main, Germany. Correspondence should be addressed to R.R. (roland.riek@phys.chem.ethz.ch).

Received 17 June; accepted 29 November; published online 26 December 2016; doi:10.1038/nsmb.3345

We attributed this to the helical character of the majority of residues yielding strong signal overlap (**Supplementary Fig. 3**), as well as the large size of the rdHDLs, which had a molecular weight of ~108 kDa and, concomitantly, a rotational tumbling time of approximately 34 ns (**Supplementary Fig. 4g**)[18]. Thus the sequential assignment analysis was limited to tr-HNCA, tr-HNCO and [^{1}H,^{1}H]-NOESY-[^{15}N,^{1}H]-HMQC spectra.

Hence, we applied an alternative approach by following a recent, thorough investigation on the scrambling of selectively unlabeled amino acids produced in the common *Escherichia coli* strain BL21(DE3)[22]. On the basis of published data and by taking into consideration the exposed scrambling pathways[22], we developed a 'three-steps-iterative' unlabeling strategy accompanied by the measurement and analysis of 2D [^{15}N,^{1}H]-TROSY, 3D tr-HNCO and 3D-NOESY-HMQC spectra (explained in detail in **Supplementary Note 1**). This approach enabled unambiguous sequential assignment to a completeness of 95% (i.e., ^{1}H, ^{15}N, ^{13}C$^\alpha$, and ^{13}CO of 158 (out of 167) residues were assigned, whereas only 90 C$^\beta$ resonances could be assigned).

The resonance assignment allows the determination of secondary structure elements. The positive ^{13}C$^\alpha$ secondary chemical shifts showed the presence of a fully formed α-helical secondary structure for residues 58–240 (**Fig. 1d** and **Supplementary Fig. 4a**)[23,24], in accordance with recent EPR experiments[25]. The nine helices formed, referred to as helices 1–10 (excluding helix 5), are S58-Q63 (helix 1),

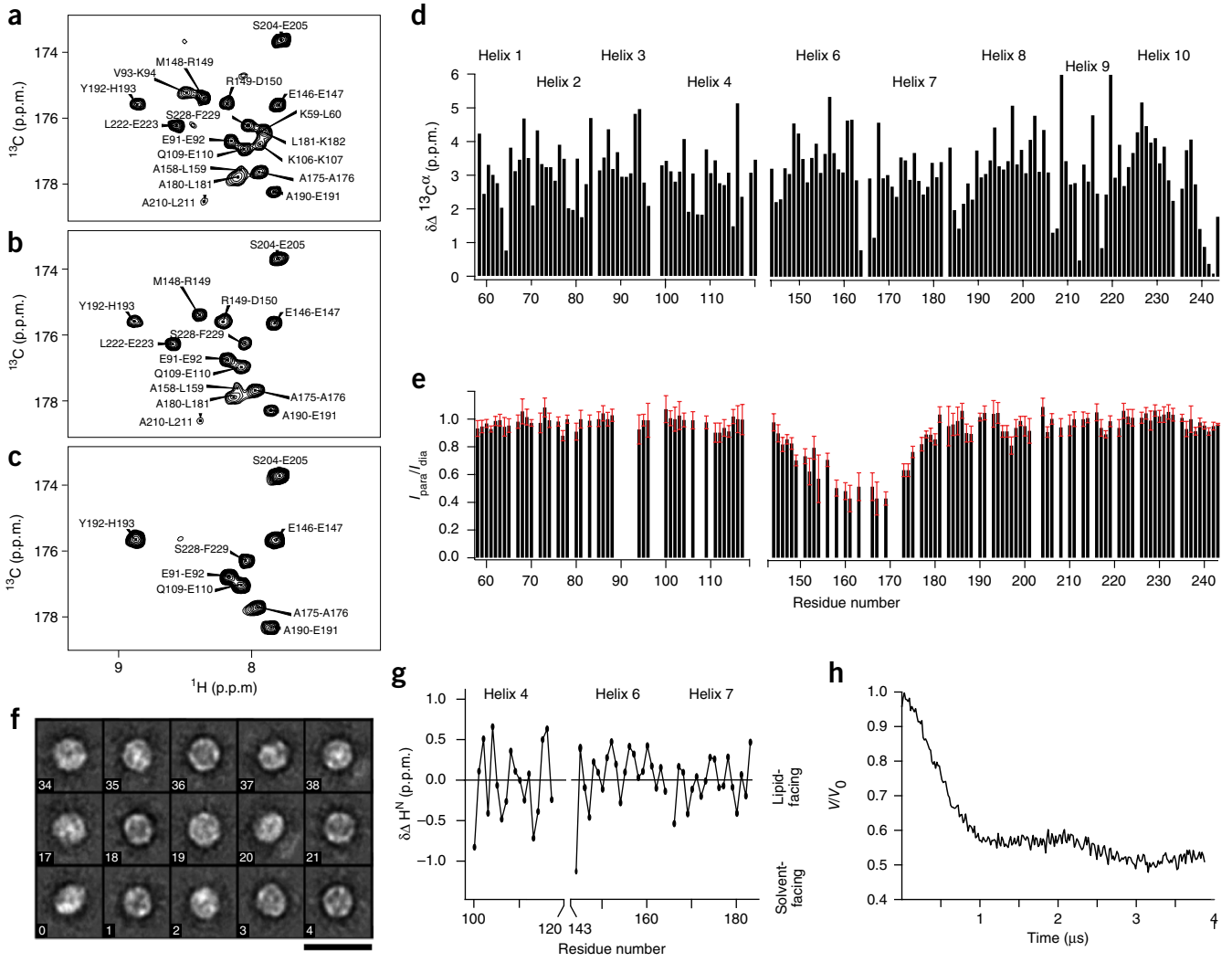

Figure 1 NMR, TEM and EPR analyses of rdHDL. (**a**) [^{13}C,^{1}H] plane of the 3D HNCO spectrum of uniformly ^{15}N,^{13}C,^{2}H-labeled rdHDL with sequential assignments at a ^{15}N chemical shift of 120.2 p.p.m. (**b**) Corresponding [^{13}C,^{1}H] plane for Lys-nonlabeled, otherwise ^{15}N,^{13}C,^{2}H-labeled rdHDL. (**c**) Corresponding [^{13}C,^{1}H] plane for Lys/Leu/Arg-nonlabeled, otherwise ^{15}N,^{13}C,^{2}H-labeled rdHDL. (**d**) Residue-specific ^{13}Cα secondary chemical shift (δΔ^{13}Cα). Positive δΔ^{13}Cα values indicate an α-helical conformation. (**e**) Intermolecular paramagnetic relaxation NMR spectroscopy data for rdHDL composed of ^{15}N-labeled MSPΔH5 and ^{14}N-labeled MSPΔH5, the latter having a paramagnetic MTSL at residue 100. The reduced cross-peak intensity ratios for residues 150–180 are due to the spatial intermolecular neighborhoods of residue 100 and residues 150–180. Error bars (s.e.m.) were calculated with Gaussian error propagation using the noise-to-signal ratios from the dia- and paramagnetic sample; one sample was used for each experiment. I_{para}, paramagnetic intensity; I_{dia}, diamagnetic intensity. (**f**) Refined negative-stain TEM pictures of rdHDLs. Scale bar, 220 Å. (**g**) Secondary amide chemical shifts δΔ^{1}H^N versus the amino acid sequences of helices 4, 6 and 7 of rdHDL. The wave pattern is attributed to the curvature of the helices, allowing the solvent- and lipid-facing sides of the helices to be determined. (**h**) Normalized phase-corrected primary electron paramagnetic DEER data versus time for rdHDL with MTSL at residue 100. The primary DEER time trace shows well-defined dipolar oscillations corresponding to a compact distance distribution.

V67-K77 (helix 2), E80-V93 (helix 3), L101-Q117 (helix 4), L144-T164 (helix 6), S167-E183 (helix 7), R188-E207 (helix 8), A210-L219 (helix 9), and V221-K239 (helix 10). They are interrupted by Pro and/or Gly residues that exhibit greater flexibility and/or small $^{13}C^{\alpha}$ secondary chemical shifts (**Supplementary Fig. 4**).

Helix bending of rdHDL particles

The secondary amide chemical shifts ($\Delta\delta H^N$) observed in NMR spectroscopy experiments revealed bending of the helices, as they showed a helical-wheel-typical wave-like pattern (**Fig. 1g** and **Supplementary Fig. 5**). This interpretation is based on the rationale that bending should result in shorter hydrogen bonds at the concave side of the helices and longer hydrogen bonds at the convex, solvent-facing side of the helices. Because amides involved in shorter hydrogen bonds show greater deshielding effects from the hydrogen bond carbonyl partner than amides involved in longer hydrogen bonds do, it is expected that the concave side of the helices may show positive secondary amide chemical shifts, whereas deshielding effects should be reduced on the convex side of the helices owing to the presence of longer hydrogen bonds, resulting in negative secondary chemical shifts[26]. For helices 3–9, a clear periodicity of three or four is found, which is usually interpreted as related to curvature[27–29]. For helix 1 the wave pattern is less obvious, highlighting the fact that helix 1 deviates somewhat in its properties (i.e., different relaxation and secondary chemical shifts) from the other helical segments. The lack of the wave pattern in helix 2 is attributed to potential ring-current shifts induced by F71 and W72. Furthermore, residues following prolines have strongly negative $\Delta\delta H^N$ throughout the entire protein, although their hydrophobic character and wave pattern would lead one to predict a positive $\Delta\delta H^N$ (**Supplementary Fig. 5**).

Finally, chemical shift analysis of rdHDLs with and without helix 5 showed similar chemical shifts, strongly indicating that the overall structure of rdHDL is preserved in the shortened construct (**Supplementary Fig. 1**). Similarly, the chemical shifts between rdHDL particles composed of MSPΔH5 and the lipid POPC (1-palmitoyl-2-oleoyl-*sn*-glycero-3-phosphocholine) and those consisting of MSPΔH5 and DMPC were similar, indicating that the 3D structure is preserved in both lipid systems (**Supplementary Fig. 5c**).

Dynamics of rdHDL particles

To assess the dynamical properties of rdHDLs in a more detailed way, we carried out five different NMR spectroscopy relaxation experiments[30,31]. Overall, the relaxation data are consistent with the notion of a well-defined structure, with [^{1}H]-^{15}N heteronuclear NOE (hetNOE) values of ~0.85 (**Supplementary Fig. 4b**), R1 values between 0.25 and 0.5 s^{-1} (**Supplementary Fig. 4c**), and order parameters S^2 in the range of 0.9 (**Supplementary Fig. 4e**). $R2_{R1\rho}$ and $R2_{\beta}$, reporting on slower timescale motions, had values between 60–80 s^{-1} and 20–30 s^{-1}, both reflecting the large size of the complex (**Supplementary Fig. 4d**,**e**). We observed deviations from the overall relaxation values for the N-terminal segment until Glu70. The relatively high R1 and low $R2_{R1\rho}$ values suggest that the N-terminal helix (helix 1) is undergoing large-amplitude rigid-body motions. Additionally, strong drops in the [^{1}H]-^{15}N hetNOE, $R2_{R1\rho}$, S^2 and η_{xy} values (**Supplementary Fig. 4g**) and, conversely, a strong increase in the R1 values indicated that the four C-terminal residues are highly flexible and unstructured.

The double-belt structure of rdHDL particles

We determined the 3D structure of rdHDL by using NOE-derived distance restraints for distances up to 10 Å, and paramagnetic relaxation enhancement (PRE)-derived and double electron-electron resonance (DEER)-derived distance restraints using MTSL (*S*-(1-oxyl-2,2,5,5-tetramethyl-2,5-dihydro-1H-pyrrol-3-yl)methyl methanesulfonothioate)-labeled rdHDL for distance restraints up to 65 Å, in combination with negative-stain TEM (**Fig. 1**, **Supplementary Figs. 2** and **6–8**, **Table 1** and Online Methods). The resulting 3D structure is represented by a bundle of ten conformers (**Fig. 2a**,**b**). It has an r.m.s. deviation of 1.17 Å for the backbone atoms of residues 70–240.

The 3D structure of rdHDL showed that two MSPΔH5 molecules encircle the DMPC bilayer in an antiparallel fashion to form a double belt, each using eight bent helices (**Fig. 2a**,**b** (DMPC bilayer not shown)). This dimeric arrangement supports the originally proposed double-belt model[32]. The helices are interrupted by short, sometimes dynamic, kinks and/or loops that contain Pro and/or Gly residues (**Fig. 2** (yellow residues) and **Supplementary Fig. 4**). Within the calculated ten conformers, the orientation of the N-terminal helix 1 varied (**Fig. 2a**,**b**).

Table 1 NMR and refinement statistics for rdHDL

	Protein (PDB 2N5E)
NMR distance and dihedral constraints	
Distance constraints	
Total NOE	856
Intraresidue	152
Inter-residue	704
Sequential ($\|i-j\|=1$)	338
Medium-range ($2\le\|i-j\|\le4$)	310
Long-range ($\|i-j\|\ge5$)	14
Intermolecular	42
Hydrogen bonds	490
Total dihedral-angle restraints	
ϕ	284
Ψ	284
Total dipolar coupling restraints	
H^N-N	222
N(i)-CO($i-1$)	188
Q-factor (Q_{free})[a]	14.93 (19.6)
Total PRE restraints	
Intramolecular	26
Intermolecular	224
Lower-distance bounds	1,794
Total EPR restraints	
Intramolecular	0
Intermolecular	6
Structure statistics[b]	
Violations (mean ± s.d.)	0
Distance constraints (Å)	
Dihedral-angle constraints (°)	
Maximum dihedral-angle violation (°)	
Maximum distance-constraint violation (Å)	
Deviations from idealized geometry	
Bond lengths (Å)	0.001
Bond angles (°)	0.2
Impropers (°)	
Average pairwise r.m.s. deviation (Å)[c]	
Heavy	1.7
Backbone	1.17

[a]Q_{free} was calculated according to ref. 43. [b]Ramachandran statistics can be found in the Online Methods. [c]Pairwise r.m.s. deviation was calculated among ten refined structures for residues 70–240.

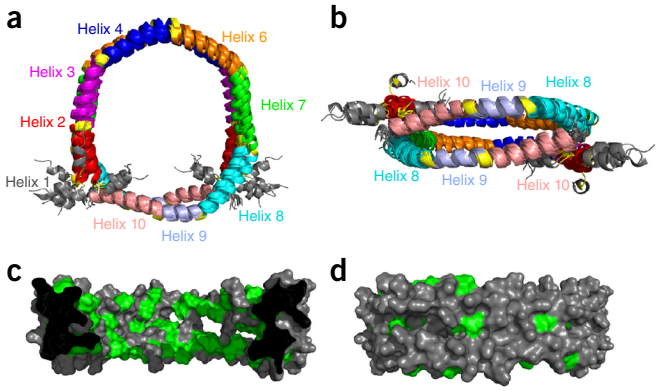

Figure 2 The double-belt 3D structure of rdHDL. (**a**,**b**) Top (**a**) and side (**b**) views of the ten conformers of rdHDL. Two antiparallel MSPΔH5 molecules encircle a lipid bilayer patch (not shown) to form a structure with two-fold symmetry. The nine helices of each monomer are individually color-coded and labeled. Pro or Gly residues (yellow) usually separate individual helices. The following helices are juxtaposed in the dimer: helix 4 with helix 6; helices 2 and 3 with helix 7; and helices 8 and 9 with helix 10. Helix 1, residues 58–63; helix 2, residues 67–77; helix 3, residues 80–93; helix 4, residues 101–117; helix 6, residues 144–164; helix 7, residues 167–183; helix 8, residues 188–207; helix 9, resides 210–219; and helix 10, residues 221–239. (**c**) Van der Waals surface representation of rdHDL cut in half to reveal the lipid-oriented interior, with hydrophobic residues colored in green. (**d**) Presentation of the solvent-exposed surface, which is removed in **c**.

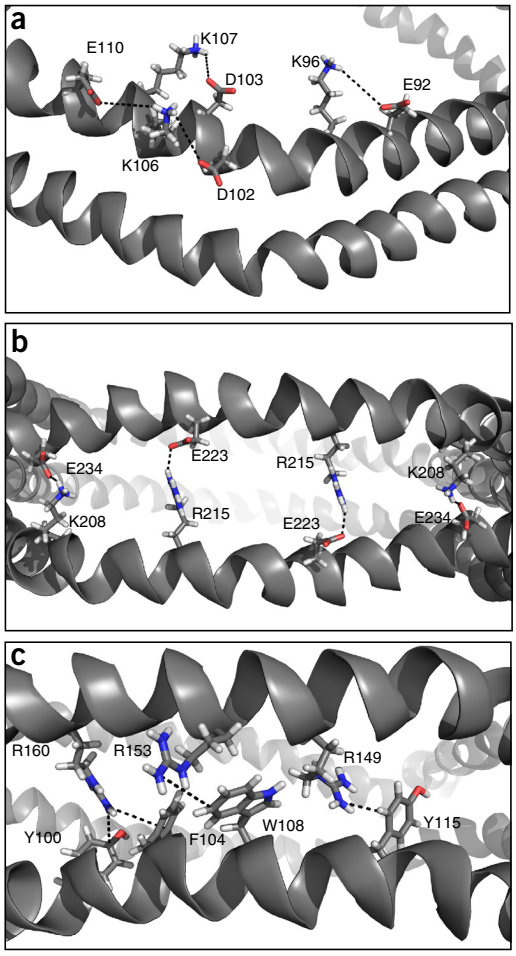

Figure 3 Salt bridges and cation-π interaction networks that determine the 3D structure of rdHDL. (**a**,**b**) Proposed intramolecular (**a**) and intermolecular (**b**) salt bridges (dashed lines). (**c**) Intermolecular cation-π interactions. Helical ribbons indicate backbones of both MSPΔH5 molecules. Stick representations show side chains of the labeled (one-letter code) residues of interest. Red, oxygen; blue, nitrogen; white, protons; gray, carbon atoms.

This is in accordance with the relaxation measurements, which showed large-amplitude motions for helix 1 (**Supplementary Fig. 4**), as discussed above. In the disc region, helix 4 of one MSPΔH5 molecule is juxtaposed against helix 6 of the other. Similarly, helices 2 and 3 are juxtaposed with helix 7, and helices 8 and 9 with helix 10. Furthermore, prolines and glycines of both molecules are often nearby (**Fig. 2**, yellow residues), allowing for intermolecular alignment of the helices. The presented arrangement, called 5/5 registry, has been found for reconstituted and human plasma discoidal and spherical HDLs[11,17,33,34], underpinning the biological relevance of the reconstituted discoidal MSPΔH5–DMPC complex.

Helix rotation after lipidation

Within the ten NMR conformers, up to 28 intra- and intermolecular salt bridges are formed simultaneously and distributed along the MSPΔH5 sequence (**Fig. 3a**,**b**). In contrast, intermolecular cation-π interactions are localized at the interface of helices 6 and 4 (**Fig. 3c**) in an arginine-zipper-like arrangement in which the side chains of Arg149, Arg153 and Arg160 of helix 6 of one MSPΔH5 molecule are located between the aromatic rings of Tyr115, Trp108, Phe104 and Tyr100 from helix 4 of the other MSPΔH5 molecule. Because negligible chemical shift changes are found for these residues in rdHDLs containing helix 5 (**Supplementary Fig. 1b**), it is assumed that the cation-π zipper is preserved in both rdHDL constructs. As a result of symmetry, the same patch is found twice, juxtaposed because of the missing segment denoted helix 5.

As expected, the lipid-oriented interior of rdHDL is hydrophobic in nature (**Fig. 2c**), in contrast to the hydrophilic solvent-exposed face (**Fig. 2d**). This arrangement finds independent support from the secondary amide chemical shifts $\Delta\delta H^N$ discussed above, which are most positive for lipid-facing amide moieties because of the shorter hydrogen bonds at the concave lipid-facing side of the bent helices (**Fig. 1g** and **Supplementary Fig. 5a**). The amphiphilic character of the helices can be described by the modified canonical heptad repeat, originally documented for soluble α-helical coiled-coil proteins[35–37]. This heptad repeat, denoted by $(abc[c']defg)_n$, starts with Thr68 and continues until Leu219 for apoA-I[35–37] (**Supplementary Fig. 5b**). In coiled-coil structures, 'a' and 'd' are nonpolar residues at the dimer interface stabilizing the structure (**Fig. 4a**). Notably, the dimerization interface for the crystal structure of dimeric lipid-free apoA-I (PDB 3R2P) corresponds exactly to the mentioned coiled-coil interface with residues 'a' and 'd' buried at the dimer interface[38] (**Fig. 4b**).

For assembled lipid-containing rdHDLs, however, the hydrophobic residues with the assigned heptad letters 'a' and 'd' are rotated toward the hydrophobic lipid bilayer, placing residues at position 'e' at the intermolecular helix-helix interface (**Fig. 4**). This orientation is known as 'right-to-right' (RR). Notably, this orientation fundamentally contradicts the computationally derived and currently accepted 'left-to-left' (LL) rotation, which places residues at position 'g' at the intermolecular helix-helix interface (see **Supplementary Fig. 9** for a detailed explanation of these differences using the simplified coloring for R residues and L residues)[32].

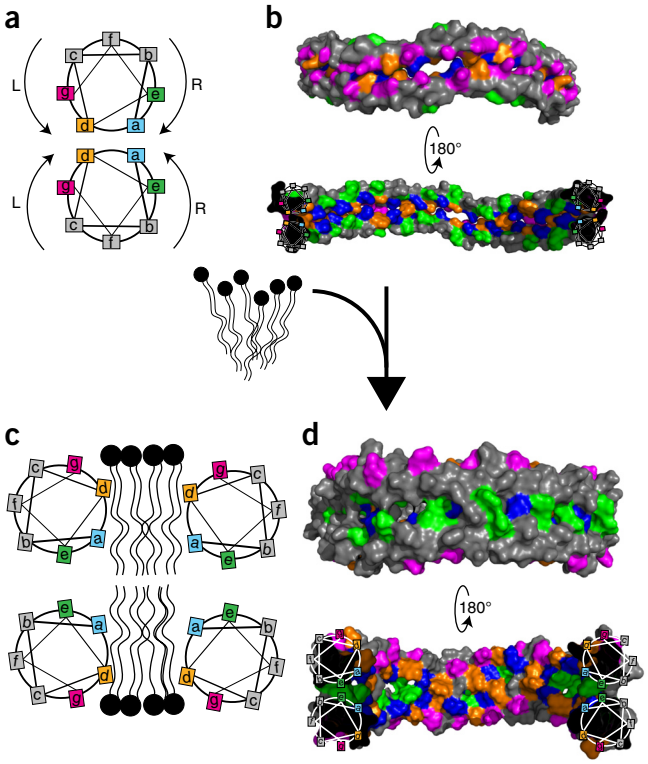

Figure 4 Structural reorganization of apoA-I from its soluble to its lipid-containing state upon RR rotation and rdHDL formation. (**a**) Helical wheel representation of two antiparallel coiled-coil helices using the canonical heptad repeat sequence $(abcdefg)_n$: nonpolar residues 'a' and 'd' are located at the interface of two helices and mediate hydrophobic interactions; polar residues 'e' and 'g' further stabilize the structure through electrostatic interactions. (**b**) Crystal structure of lipid-free dimeric apoA-I (PDB 3R2P). Hydrophobic residues (color-coded according to **a**) are found at the dimerization interface and stabilize the soluble dimeric form of apoA-I. This results in a distribution of 'e' residues on one side and 'g' residues on the other side as found for α-helical coiled-coil structures. (**c**) As indicated in **a**, after lipidation and assembly into discoidal HDL particles, both helices can undergo either RR rotation, positioning residue 'e' at the dimer interface, or LL rotation, positioning residue 'g' at the dimer interface, to expose the hydrophobic residues to the lipid bilayer. (**d**) In rdHDLs, the helices rotate RR so that hydrophobic residues at positions 'a' and 'd' can face the lipid bilayer (bottom structure, showing the lipid-containing interior of the rdHDL particle). The RR rotation of the protein after rdHDL formation places the 'e' residues (green) at the dimer interface (upper structure; the outside part of the rdHDL particle, which is removed in the lower structure, is shown). The 'g' residues are solvent-exposed and oriented toward the lipid head groups.

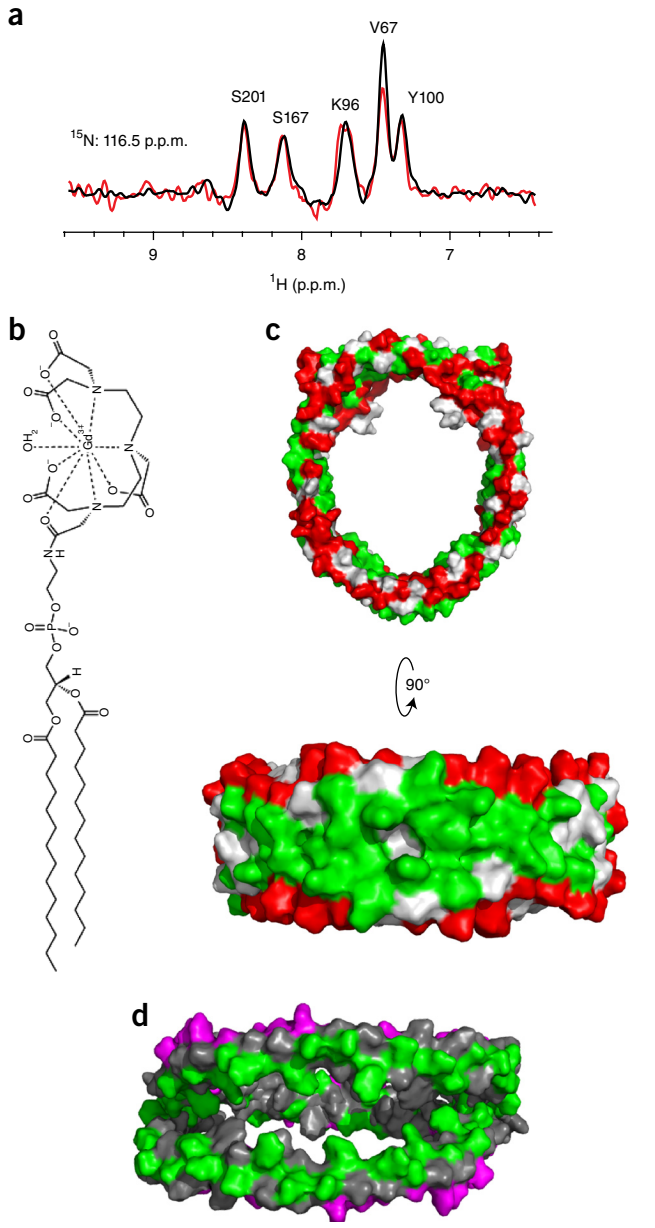

Figure 5 Experimental verification of the proposed RR rotation. (**a**) 1D trace of 2D [^{15}N,^{1}H]-TROSY-HSQC at 116.5 p.p.m. (^{15}N frequency), demonstrating the selective signal broadening for the lipid PRE experiment. The spectrum represented by the black trace does not contain any gadolinium-tagged PE-DTPA, whereas the spectrum shown by the red trace does. (**b**) Representation of the used lipid, PE-DTPA, containing a gadolinium ion that is bound to the head group. (**c**) Lipid PRE experiments underpin the RR rotation. Lipids with a gadolinium-containing head group reduce signal intensities of residues close to the lipid head groups. Residues located farther away—for example, at the dimer interface—should be affected only slightly or not at all. Residues that show significant broadening are colored in red, whereas residues with no or little broadening are colored in green (for residues colored white, no intensity ratio could be assigned). (**d**) Rigid-body docking using an unrestricted grid search results in the RR rotation when only the six EPR long-range restraints are used. For docking, no NMR restraints between the two apoA-I protomers were included (see **Supplementary Note 1** for more information). Color-coded according to the RR and LL color-coding from ref. 32, which shows an 11-mer helical wheel representation in which residues at positions 2, 9 and 5 are designated as 'left' (L, colored pink), and residues at positions 1, 4 and 7 are designated as 'right' (R, colored green) (see **Supplementary Fig. 9** for more information).

We obtained independent corroboration for the RR rotation from lipid PRE experiments (**Fig. 5a–c**) and from rigid-body docking on the basis of EPR restraints (**Fig. 5d**; see **Supplementary Note 1** for further information regarding the rigid-body docking). Furthermore, lipid PRE experiments for HDL particles with and without helix 5 showed a similar broadening pattern (**Supplementary Fig. 1e**), underpinning the fact that the rotational state of rdHDLs is preserved in both constructs and does not depend on the presence of helix 5.

DISCUSSION

The presented 3D structure of the rdHDL (**Figs. 2** and **3**) with its two antiparallel-oriented bent helical apoA-I molecules, which embrace the lipid bilayer with a hydrophobic face and which interact by a set of salt bridges and a cation-π zipper motifs, sheds light on the formation

and function of HDL as a container for shuttling cholesterol and lipids. In particular, the structural comparison between the X-ray crystal structure of soluble apoA-I and the presented rdHDL structure (**Fig. 4b**,**d**) shows that the required structural rearrangement from a soluble lipid-free protein dimer into a membrane container includes rotation of the helices such that the hydrophobic side chains at positions 'a' and 'd', buried in the protein-protein interface in the soluble lipid-free state, face the lipid bilayer in the rdHDL particle. In contrast to findings from earlier studies based on molecular dynamics simulation[32], an RR rotation is thus necessary (**Fig. 4** and **Supplementary Fig. 9**) so that the hydrophobic residues at positions 'a' and 'd' can accommodate the lipid bilayer, while intermolecular helix-helix interactions are stabilized via contacts through residues at position 'e'. In particular, up to 28 salt bridges and the above-mentioned cation-π interactions between helices 6 and 4 stabilize this structural arrangement, which seems to be independent of helix 5. Notably, the amino acid sequence with its extensive amphiphilic character also enables the lipid-free apoA-I dimers to be water soluble. The extraordinary cation-π-stacking zipper between helices 4 and 6, whose participating residues are highly conserved in mammals and birds[39], is the most notable unique feature of the structure.

Furthermore, helix 6 (residues 144–164) has an important role in HDL metabolism; considerable evidence suggests that helix 6 of apoA-I is the major target for LCAT binding, which is crucial for cholesterol uptake and modification, and concomitantly maturation to spherical HDLs. Given that spherical HDLs are much longer-lived in blood plasma than discoidal HDL[40,41], it is not surprising that in a naturally occurring deletion mutant missing residues 146–160, plasma HDL levels were reduced ten times[42], or that 12 of 17 mutations known to reduce plasma HDL concentration are located in helix 6 (**Supplementary Fig. 10**).

The 3D HDL structure presented here is a fascinating representation of how nature highly economically solved the problem of efficiently shuttling hydrophobic molecules and lipids between tissues in a hydrophilic environment. Because of their circular dimerization, two apoA-I molecules are capable of bundling ~100 lipid molecules at once in a cargo that is transported in the hydrophilic environment in its naturally occurring and energetically favorable bilayer state with immersed hydrophobic molecules as a whole.

METHODS

Methods, including statements of data availability and any associated accession codes and references, are available in the online version of the paper.

Note: Any Supplementary Information and Source Data files are available in the online version of the paper.

ACKNOWLEDGMENTS

We thank N.A. Lakomek and S.A. Müller for insightful discussions and critical reading of the manuscript. This work was supported by the ETH fellowship program, financed by the ETH Zurich and the EU COFUND program under award number FEL-2012-1 (to S.B.); the Swedish research council (Ventenskap Rådet VR-2011-13 to C.N.C.); Wenner-Gren Stiftelsern WG-13 (to C.N.C.); the NCCR TransCure (H.S.); the SNF (grant 205320_166164 to H.S., grant 200020_157034 to G.J., and grant 144444 to R.R.); and Eurostars grant E! 9803 funded by the State Secretariat for Education, Research and Innovation of the Swiss Confederation (to P.G.). Plasmid pET-28a was a generous gift from the Zerbe lab (University of Zurich, Zurich, Switzerland) given with permission from G. Wagner (Harvard University, Cambridge, Massachusetts, USA).

AUTHOR CONTRIBUTIONS

S.B. produced the protein, and recorded and analyzed all NMR data; Y.P. and G.J. recorded and analyzed the EPR data; C.E. produced the protein; C.N.C. produced the mutations; J.K., S.A., R.A.M. and H.S. recorded and analyzed electron microscopy data; P.G. helped with the structure calculation; and S.B. and R.R. discussed the data and wrote the paper. All authors discussed the results.

COMPETING FINANCIAL INTERESTS

The authors declare no competing financial interests.

1. Zannis, V.I. *et al.* HDL biogenesis, remodeling, and catabolism. *Handb. Exp. Pharmacol.* **224**, 53–111 (2015).
2. Kingwell, B.A. & Chapman, M.J. Future of high-density lipoprotein infusion therapies: potential for clinical management of vascular disease. *Circulation* **128**, 1112–1121 (2013).
3. Navab, M., Reddy, S.T., Van Lenten, B.J. & Fogelman, A.M. HDL and cardiovascular disease: atherogenic and atheroprotective mechanisms. *Nat. Rev. Cardiol.* **8**, 222–232 (2011).
4. Kingwell, B.A., Chapman, M.J., Kontush, A. & Miller, N.E. HDL-targeted therapies: progress, failures and future. *Nat. Rev. Drug Discov.* **13**, 445–464 (2014).
5. Kontush, A. *et al.* Structure of HDL: particle subclasses and molecular components. *Handb. Exp. Pharmacol.* **224**, 3–51 (2015).
6. Rogers, D.P. *et al.* Truncation of the amino terminus of human apolipoprotein A-I substantially alters only the lipid-free conformation. *Biochemistry* **36**, 288–300 (1997).
7. Segrest, J.P., Garber, D.W., Brouillette, C.G., Harvey, S.C. & Anantharamaiah, G.M. The amphipathic alpha helix: a multifunctional structural motif in plasma apolipoproteins. *Adv. Protein Chem.* **45**, 303–369 (1994).
8. Segrest, J.P. *et al.* The amphipathic helix in the exchangeable apolipoproteins: a review of secondary structure and function. *J. Lipid Res.* **33**, 141–166 (1992).
9. Gursky, O. Crystal structure of Δ(185-243)ApoA-I suggests a mechanistic framework for the protein adaptation to the changing lipid load in good cholesterol: from flatland to sphereland via double belt, belt buckle, double hairpin and trefoil/tetrafoil. *J. Mol. Biol.* **425**, 1–16 (2013).
10. Denisov, I.G., Grinkova, Y.V., Lazarides, A.A. & Sligar, S.G. Directed self-assembly of monodisperse phospholipid bilayer Nanodiscs with controlled size. *J. Am. Chem. Soc.* **126**, 3477–3487 (2004).
11. Silva, R.A.G.D. *et al.* Structure of apolipoprotein A-I in spherical high density lipoproteins of different sizes. *Proc. Natl. Acad. Sci. USA* **105**, 12176–12181 (2008).
12. Asztalos, B.F. *et al.* Role of LCAT in HDL remodeling: investigation of LCAT deficiency states. *J. Lipid Res.* **48**, 592–599 (2007).
13. Zannis, V.I., Chroni, A. & Krieger, M. Role of apoA-I, ABCA1, LCAT, and SR-BI in the biogenesis of HDL. *J. Mol. Med.* **84**, 276–294 (2006).
14. Gauthamadasa, K. *et al.* Speciated human high-density lipoprotein protein proximity profiles. *Biochemistry* **49**, 10656–10665 (2010).
15. Bruce, C., Chouinard, R.A. Jr. & Tall, A.R. Plasma lipid transfer proteins, high-density lipoproteins, and reverse cholesterol transport. *Annu. Rev. Nutr.* **18**, 297–330 (1998).
16. Qiu, X. *et al.* Crystal structure of cholesteryl ester transfer protein reveals a long tunnel and four bound lipid molecules. *Nat. Struct. Mol. Biol.* **14**, 106–113 (2007).
17. Huang, R. *et al.* Apolipoprotein A-I structural organization in high-density lipoproteins isolated from human plasma. *Nat. Struct. Mol. Biol.* **18**, 416–422 (2011).
18. Hagn, F., Etzkorn, M., Raschle, T. & Wagner, G. Optimized phospholipid bilayer nanodiscs facilitate high-resolution structure determination of membrane proteins. *J. Am. Chem. Soc.* **135**, 1919–1925 (2013).
19. Bibow, S. *et al.* Measuring membrane protein bond orientations in nanodiscs via residual dipolar couplings. *Protein Sci.* **23**, 851–856 (2014).
20. Frey, L., Lakomek, N.A., Riek, R. & Bibow, S. Micelles, bicelles, and nanodiscs: comparing the impact of membrane mimetics on membrane protein backbone dynamics. *Angew. Chem. Int. Ed. Engl.* http://dx.doi.org/10.1002/anie.201608246 (2016).
21. Salzmann, M., Wider, G., Pervushin, K., Senn, H. & Wuthrich, K. TROSY-type triple-resonance experiments for sequential NMR assignments of large proteins. *J. Am. Chem. Soc.* **121**, 844–848 (1999).
22. Bellstedt, P. *et al.* Resonance assignment for a particularly challenging protein based on systematic unlabeling of amino acids to complement incomplete NMR data sets. *J. Biomol. NMR* **57**, 65–72 (2013).
23. Spera, S. & Bax, A. Empirical correlation between protein backbone conformation and Cα and Cβ ^{13}C nuclear magnetic resonance chemical shifts. *J. Am. Chem. Soc.* **113**, 5490–5492 (1991).
24. Wishart, D.S. & Sykes, B.D. Chemical shifts as a tool for structure determination. *Methods Enzymol.* **239**, 363–392 (1994).
25. Oda, M.N. *et al.* The secondary structure of apolipoprotein A-I on 9.6-nm reconstituted high-density lipoprotein determined by EPR spectroscopy. *FEBS J.* **280**, 3416–3424 (2013).
26. Zhou, N.E., Zhu, B.Y., Sykes, B.D. & Hodges, R.S. Relationship between amide proton chemical-shifts and hydrogen-bonding in amphipathic α-helical peptides. *J. Am. Chem. Soc.* **114**, 4320–4326 (1992).

27. Blanco, F.J. *et al.* NMR chemical shifts: a tool to characterize distortions of peptide and protein helices. *J. Am. Chem. Soc.* **114**, 9676–9677 (1992).
28. Bracken, C., Carr, P.A., Cavanagh, J. & Palmer, A.G. III. Temperature dependence of intramolecular dynamics of the basic leucine zipper of GCN4: implications for the entropy of association with DNA. *J. Mol. Biol.* **285**, 2133–2146 (1999).
29. Kuntz, I., Kosen, P. & Craig, E. Amide chemical shifts in many helices in peptides and proteins are periodic. *J. Am. Chem. Soc.* **113**, 1406–1408 (1991).
30. Lakomek, N.A., Ying, J. & Bax, A. Measurement of ^{15}N relaxation rates in perdeuterated proteins by TROSY-based methods. *J. Biomol. NMR* **53**, 209–221 (2012).
31. Lakomek, N.A. *et al.* Internal dynamics of the homotrimeric HIV-1 viral coat protein gp41 on multiple time scales. *Angew. Chem. Int. Ed. Engl.* **52**, 3911–3915 (2013).
32. Segrest, J.P. *et al.* A detailed molecular belt model for apolipoprotein A-I in discoidal high density lipoprotein. *J. Biol. Chem.* **274**, 31755–31758 (1999).
33. Phillips, M.C. New insights into the determination of HDL structure by apolipoproteins. *J. Lipid Res.* **54**, 2034–2048 (2013).
34. Thomas, M.J., Bhat, S. & Sorci-Thomas, M.G. Three-dimensional models of HDL apoA-I: implications for its assembly and function. *J. Lipid Res.* **49**, 1875–1883 (2008).
35. Borhani, D.W., Rogers, D.P., Engler, J.A. & Brouillette, C.G. Crystal structure of truncated human apolipoprotein A-I suggests a lipid-bound conformation. *Proc. Natl. Acad. Sci. USA* **94**, 12291–12296 (1997).
36. Mason, J.M. & Arndt, K.M. Coiled coil domains: stability, specificity, and biological implications. *ChemBioChem* **5**, 170–176 (2004).
37. Nolte, R.T. & Atkinson, D. Conformational analysis of apolipoprotein A-I and E-3 based on primary sequence and circular dichroism. *Biophys. J.* **63**, 1221–1239 (1992).
38. Mei, X. & Atkinson, D. Crystal structure of C-terminal truncated apolipoprotein A-I reveals the assembly of high density lipoprotein (HDL) by dimerization. *J. Biol. Chem.* **286**, 38570–38582 (2011).
39. Bashtovyy, D., Jones, M.K., Anantharamaiah, G.M. & Segrest, J.P. Sequence conservation of apolipoprotein A-I affords novel insights into HDL structure-function. *J. Lipid Res.* **52**, 435–450 (2011).
40. Sorci-Thomas, M.G., Bhat, S. & Thomas, M.J. Activation of lecithin: cholesterol acyltransferase by HDL ApoA-I central helices. *Clin. Lipidol.* **4**, 113–124 (2009).
41. Glukhova, A. *et al.* Structure and function of lysosomal phospholipase A2 and lecithin: cholesterol acyltransferase. *Nat. Commun.* **6**, 6250 (2015).
42. Sorci-Thomas, M.G. & Thomas, M.J. The effects of altered apolipoprotein A-I structure on plasma HDL concentration. *Trends Cardiovasc. Med.* **12**, 121–128 (2002).
43. Clore, G.M. & Garrett, D.S. *R*-factor, free *R*, and complete cross-validation for dipolar coupling refinement of NMR structures. *J. Am. Chem. Soc.* **121**, 9008–9012 (1999).

ONLINE METHODS

Expression, purification and formation of rdHDL particles. The plasmid pET-28a with the coding sequence of truncated apoA-I missing residues 1–54 and 121–142 (MSPΔH5), with an N-terminal tobacco etch virus protease–cleavable histidine tag, was a generous gift from the Zerbe lab (University of Zurich) given with permission from Gerhard Wagner (Harvard University). To obtain the triple-labeled MSPΔH5 required for sequential resonance assignment experiments, we expressed the plasmid in *E. coli* strain BL21(DE3) Star (Invitrogen) in Terrific Broth at 37 °C until OD_{600} = 0.8. Cells were centrifuged at 5,000*g* for 10 min at 23 °C and subsequently resuspended in M9 minimal medium containing 2 g/L $^{15}NH_4Cl$ and 3–4 g/L ^{13}C-labeled D-glucose and 90% D_2O (ref. 44). The incubator temperature was changed to 28 °C, and after 1 h protein overproduction was initiated by the addition of 0.3 mM isopropyl β-D-1-thiogalactopyranoside (IPTG; Invitrogen). The cultures were then incubated at 28 °C for 8 h.

In addition to uniformly $^{2}H,^{13}C,^{15}N$-labeled MSPΔH5, ten different selectively unlabeled MSPΔH5 samples were produced, containing the NMR-invisible isotopes ^{12}C and ^{14}N for alanine, arginine, asparagine, glutamine, histidine, leucine, lysine, threonine and valine, as well as for the combined lysine/leucine/arginine-unlabeled sample. To obtain selectively unlabeled samples, we added 800 mg/L of the respective $^{1}H,^{12}C,^{14}N$ amino acid(s) to the isotope-containing M9 minimal medium the day before cells were grown and dissolved it by shaking overnight. Cells were harvested by centrifugation at 5,000*g* for 10 min at 4 °C. The cell pellet was resuspended in 100 mL of buffer A (20 mM Tris-HCl, pH 8.0, 0.5 M NaCl) containing 5 mg of DNase I (Sigma) and protease inhibitor cocktail tablets, and incubated at 4 °C with gentle stirring for 20 min. 1% Triton X-100 was added to the cell suspension, and the solution was incubated with gentle stirring for another 20 min at room temperature. Afterward, the cells were destroyed using a microfluidizer operated at 40,000 p.s.i. The lysate was clarified by centrifugation at 20,000*g* for 30 min, applied to 5 mL of Ni^{2+} resin (Qiagen), and equilibrated with buffer A containing 1% Triton X-100. The column was sequentially washed with 150 mL of buffer A containing 1% Triton X-100, 150 mL of buffer A containing 50 mM of sodium cholate, 150 mL of buffer A, and finally 100 mL of buffer A containing 50 mM imidazole. MSPΔH5 was eluted with buffer A containing 0.5 M imidazole. The buffer solubilizing the purified MSPΔH5 was changed to 10 mM Tris-HCl, pH 7.4, containing 100 mM NaCl and 1 mM EDTA (NMR buffer) using a PD-10 column. Protein purity was checked by SDS–PAGE.

The N-terminal His-tag was proteolytically cleaved from MSPΔH5 by the addition of tobacco etch virus protease and overnight incubation at room temperature. The solution was applied to a Co^{2+} resin (Talon-resin, Clontech). The flow-through containing His-tag-free MSPΔH5 (checked by SDS–PAGE) was collected and subsequently concentrated with an Amicon Ultra-4 10,000-Da molecular-weight cutoff (MWCO) concentrator (Millipore) to ~550–650 μM.

For the side chain resonance assignment of Val and Leu methyl resonances, triple-labeled MSPΔH5 was grown in minimal medium with 90% D_2O overnight at 37 °C. 1 h before induction (at OD of approximately 0.7), 100 mg/L ketoisovaleric acid (CDLM-8100, Cambridge Isotope Labs) was added. For experiments regarding methyl-NOEs, $^{2}H,^{12}C,^{15}N$-labeled MSPΔH5 was prepared by the addition of 100 mg/L ketoisovaleric acid (CDLM-7317, Cambridge Isotope Labs) 1 h before induction. For the stereospecific assignment of the methyl groups, ethyl-2-hydroxy-2-methyl-^{13}C-3-oxobutanoate (Sigma-Aldrich, Switzerland) was purchased and used to obtain 2-^{13}C-methyl-4-$^{2}H_3$-acetolactate as described previously[45]; we monitored the reaction by recording 1D NMR spectra. The 2-^{13}C-methyl-4-$^{2}H_3$-acetolactate was added to the cell culture (in M9 minimal medium) 1 h before induction in the same way as the other additives[45]. The samples had a concentration of ~550–650 μM.

Deuterated d_{54}-DMPC (FBReagents) was solubilized in sodium cholate (cholate:DMPC concentration, 200:100 mM) in a glass vial. MSPΔH5 in NMR buffer was mixed with the cholate:DMPC solution at a ratio of 1:50 (MSPΔH5:DMPC) and incubated with shaking for 1–2 h at 27 °C. Formation of rdHDL particles was initiated by the addition of 1 mg of BioBeads SM2 (Bio-Rad) per 1 mL of solution. After 2–4 h the solution was separated from the BioBeads by gentle centrifugation. The formed particles were purified by size-exclusion chromatography at a flow rate of 0.5 mL/min on a Superdex 200 10/300GL gel filtration column (GE Healthcare) equilibrated with NMR buffer, and concentrated using a 10-kDa MWCO concentrator. For MSP1, expression, purification, formation and concentration were similar to those for MSPΔH5, except that the MSP1:lipid ratio was changed to 1:80.

Sample preparation for PRE and EPR experiments. To attach paramagnetic MTSL and its diamagnetic analog (Toronto Research Chemicals), we introduced cysteine mutations into the cysteine-free wild-type MSPΔH5 at positions 67, 100, 148, 166, 192, 213 and 235 using either the QuickChange site-directed mutagenesis kit (Agilent Technologies) or a standard site-directed mutagenesis protocol. Oligomers were purchased from Microsynth (Switzerland). All mutations were confirmed by sequencing. $^{15}N,^{2}H$-Cys-containing MSPΔH5 proteins were produced as described above. Corresponding $^{14}N,^{1}H$-Cys-containing MSPΔH5 proteins were produced in Terrific Broth medium as described previously[19], and purified as described above. MTSL was dissolved in DMSO, and a ten-fold excess of MTSL or its diamagnetic analog relative to the protein concentration was used for para- or diamagnetic sample preparations, respectively. The highest (90–95%) labeling efficiency was achieved when Cys-containing MSPΔH5 was dripped from a PD10 desalting column into buffer containing a ten-fold excess of MTSL. The solution was left overnight at room temperature with agitation. The next day, the remaining free MTSL was removed with a PD10 column. We achieved rdHDL assembly by mixing $^{15}N,^{2}H$-MTSL-containing MSPΔH5 with ^{14}N-^{1}H-wild-type MSPΔH5 at a ratio of 1:4 to investigate intramolecular PRE effects. The 1:4 ratio was used to reduce significant perturbation from intermolecular PRE effects. We investigated intermolecular PRE effects by assembling rdHDL in the presence of a 3:1 $^{14}N,^{1}H$-MTSL-containing MSPΔH5:$^{15}N,^{2}H$-wild-type MSPΔH5 mixture. Para- and diamagnetic MTSL-containing MSPΔH5 were produced in parallel using the same batch. The final NMR spectroscopy samples contained ~60 μM NMR-visible $^{15}N,^{2}H$-labeled MSPΔH5 within rdHDLs, corresponding to an MTSL-labeled MSPΔH5 concentration of ~60 μM for the 'intramolecular PRE' samples and 150 μM MTSL-labeled MSPΔH5 for the 'intermolecular PRE' samples. This approach is a compromise between reducing inter-HDL particle interactions (i.e., reducing paramagnetic broadening) and recording good-quality spectra in a reasonable amount of time. For EPR, pure $^{14}N,^{1}H$-MTSL-containing MSPΔH5 rdHDLs were assembled as described above. All the samples were purified by size-exclusion chromatography at a flow rate of 0.5 mL/min on a Superdex 200 10/300GL gel filtration column (GE Healthcare) equilibrated with NMR buffer, and concentrated using a 10-kDa MWCO concentrator.

For lipid-PRE experiments, gadolinium-tagged PE-DTPA (1,2-dimyristoyl-*sn*-glycero-3-phosphoethanolamine-N-diethylenetriaminepentaacetic acid, from Avanti Polar Lipids) was mixed with deuterated d_{54}-DMPC at a ratio of 1:100. Assembly for MSPΔH5 and MSP1 was done as described above. The samples were concentrated to 100 μM.

NMR spectroscopy experiments. All experiments were recorded at 316 K. All TROSY-based (tr) HNCO experiments were recorded on a Bruker DRX 600-MHz spectrometer with a cryogenic probe head. We adjusted the number of scans for each sample individually to achieve a satisfactory signal-to-noise ratio. In general, the experimental time for each tr-HNCO was between 2 and 3 d. The tr-HNCA, tr-HNCACB and [$^{1}H,^{1}H$]-NOESY-[$^{15}N,^{1}H$]-HMQC for the uniformly labeled and selectively lysine/leucine/arginine-unlabeled rdHDL samples were recorded on a 900-MHz Bruker Avance III HD spectrometer equipped with a cryogenic probe head. The NOESY mixing time was set to 150 ms and 210 ms for the uniformly labeled and selectively lysine/leucine/arginine-unlabeled rdHDL samples, respectively.

The relaxation measurements[30,31] were recorded on a 900-MHz Bruker Avance III HD spectrometer or on a Bruker AVIII 700-MHz spectrometer, both equipped with a cryogenic probe head. All relaxation experiments were recorded in an interleaved manner. For the R1 and R1ρ experiments, the relaxation decay was sampled for eight different delay durations, which were pseudorandomized (R1 delays, 0, 1,000 ms, 600 ms, 1,400 ms, 400 ms, 1,200 ms, 1,600 ms, 800 ms; R1ρ delays, 1 ms, 15 ms, 30 ms, 6 ms, 25 ms, 10 ms, 20 ms, 8 ms) with a recovery delay of 3 s for R1 and 1.5 s for R1ρ, respectively. The strength of the spin-lock field during the R1ρ measurement was 2,000 Hz. We calculated R2 rates from the R1ρ measurement by correcting the off-resonance tilted field using the relation $R2 = R1\rho/\sin 2\theta - R1/\tan 2\theta$, with $\theta = \tan^{-1}(\omega/\Omega)$, where ω is the spin-lock field strength and Ω is the offset from the ^{15}N carrier frequency. To study transverse relaxation of the slowly relaxing component ($R2_\beta$), we sampled four delays (0 ms,

doi:10.1038/nsmb.3345

50 ms, 20 ms and 30 ms) with a recovery delay of 3 s, whereas for the fast-relaxing component ($R2_\alpha$) we sampled two delays (0 and 10 ms), resulting in an intensity reduction to approximately e^{-1} (i.e., 36%). The residue-specific tumbling time τ_c was calculated according to ref. 46; η_{xy} was obtained from the difference between $R2_\alpha$ and $R2_\beta$. The $[^1H]^{15}N$-hetNOE and reference spectra were recorded with a 10-s ^1H saturation time for the NOE experiment and the equivalent recovery time for the reference experiment, each preceded by an additional 1-s recovery time. Random coil chemical shifts were calculated for a perdeuterated protein at a temperature of 42 °C and a pH of 7.4, using the database from the University of Copenhagen (http://www1.bio.ku.dk/english/research/bms/research/sbinlab/groups/mak/randomcoil/script/).

Temperatures on all used spectrometers were calibrated using the same 99.8% methanol-d4 sample. Chemical shift corrections were made using DSS. We used TALOS-N[47] to predict secondary structure, using the $^1H^N$, ^{15}N, ^{13}CO and $^{13}C^\alpha$ chemical shifts.

For PRE broadening profiles, we recorded 2D $[^{15}N,^1H]$-TROSY experiments with samples containing either paramagnetic MTSL or its diamagnetic analog as the reference. Every experiment took 24–36 h because of the low concentration of the isotope-labeled samples. Intensity ratios (I_{para}/I_{dia}) were calculated. The error was estimated using Gaussian error propagation. We converted intensity ratios to distances using the approach from Battiste and Wagner[48]. More specifically, paramagnetic R2 ($R2^{para}$) was calculated in the following way:

$$\frac{I_{para}}{I_{dia}} = \frac{R2 \times e^{-R2^{para} t}}{R2 + R2^{para}}$$

where R2 is the measured residue-specific exchange-free transverse relaxation rate (R1ρ), and t is the INEPT delay. The equation was solved with Mathematica 7. The obtained $R2^{para}$ was used to calculate the distance r:

$$r = 6\sqrt{\frac{K}{R2^{para}}\left(4\tau_c + \frac{3\tau_c}{1+\omega_H^2 * \tau_c^2}\right)}$$

using residue-specific τ_c (obtained from η_{xy}), the proton Larmor frequency ω, and 1.23×10^{-23} cm^6 s^{-2} for the constant K. These distances were defined to be between amide protons and the C^α dummy atom representing the N-O nitroxide moiety using the rotamer approach (see "EPR experiments, data processing and restraint determination").

For the lipid-PRE broadening, we recorded 2D $[^{15}N,^1H]$-TROSY experiments with samples either containing gadolinium-tagged PE-DTPA with deuterated d_{54}-DMPC or without gadolinium-tagged PE-DTPA. The interscan delay was set to 8 s. Every experiment took 48–72 h because of the low concentration of the isotope-labeled samples (~130 μM) and the long interscan delay. Intensity ratios ($I_0/I_{PE\text{-}DTPA}$) were calculated.

For the presaturation experiments, a standard $[^{15}N,^1H]$-TROSY pulse sequence was modified to include presaturation during the interscan delay of 1 s. The presaturation power used was 60 Hz on the 900-MHz spectrometer and 40 Hz on the 600-MHz spectrometer. The protein concentration was 350 μM. The intensity I_{presat} was divided by $I_{no\text{-}presat}$ (same sequence but with the presaturation power reduced by 120 dB).

The following experiments were carried out to allow sequence-specific assignment of the methyl resonances of rdHDL: The H^mC^m[CG]CBCA was recorded with 768 × 50 × 120 points ($H \times C^m \times C^{\alpha/\beta}$) and 32 scans,and the H^mC^m[CGCBCA]CO was recorded with 768 × 72 × 50 points ($H \times C^m \times CO$) and 64 scans. The H^m[CmCGCBCA]NH and [H^m]Cm[CGCBCA]NH were recorded with 768 × 64 × 64 points ($H^N \times C^m \times H^m$) and 128 scans. All experiments were recorded on a 600-MHz Avance III HD spectrometer. To investigate possible $^{13}CH_3$-$^{13}CH_3$ NOEs, we recorded a 3D ^{13}C,^{13}C-separated HMQC-NOESY-HMQC (48 increments in both indirect carbon dimensions) with a mixing time of 400 ms and 64 scans. For $^1H^N$-$^{13}CH_3$ NOEs, we recorded a 3D ^{15}N,^{13}C-separated HMQC-NOESY-HSQC (76 increments for C^m and 58 increments for ^{15}N; number of scans: 40) with a 500-ms mixing time, as well as a 3D ^{15}N-separated NOESY-HMQC with a 250-ms mixing time, 2,048 × 512 × 80 points and 4 scans.

All NMR spectra were processed with either TopSpin 3.2 (Bruker) or NMRPipe and were analyzed with SPARKY or NMRPipe.

For residual dipolar coupling (RDC) experiments, Pf1 phages were bought from Asla Biotech and used as delivered. It was important to thoroughly mix the protein-phage solution for an extended amount of time (~30 min) to homogenize the solution. Samples were measured at 316 K. The final solution contained 10 mg/mL phages in NMR buffer (100 mM NaCl), resulting in a quadrupolar deuterium splitting of D_2O of 5.7 Hz. 3D tr-HNCO experiments[49] for RDCs were recorded on a Bruker DRX 600-MHz spectrometer equipped with a cryogenically cooled probe head in an interleaved manner with 80 increments in the nitrogen dimension and 40 increments in the ^{13}C dimension, and split in the ^{15}N dimension with TopSpin 3.1. The 3D experiments allowed the collection of one-bond $^1H^N(i)$-$^{15}N(i)$ and $^{15}N(i)$-$^{15}CO(i-1)$ couplings as well as two-bond $^1H^N(i)$-$^{13}CO(i-1)$ couplings. $^1H^N$-^{15}N and ^{15}N-^{13}CO one-bond RDCs ranging from −6 Hz to +26 Hz and −8 to +6 Hz, respectively, were collected. However, because of the small magnitude of the two-bond couplings and the large molecular weight of the rdHDL particle (~100 kDa), the two-bond couplings could not be determined with sufficient accuracy. The concentration was 550–650 μM. RDCs were cross-validated according to the method proposed by Clore and Garrett[43]. We randomly removed 10% (testing data set) from the full RDC data set ten times. We then calculated the structure again ten times with the remaining 90% of the RDCs (working data set) and calculated from each structure the Q factor between omitted-but-observed and predicted RDCs (Q_{free}) by using

$$Q = \frac{\text{r.m.s.}\,(D^{measured} - D^{observed})}{\text{r.m.s.}\,(D^{observed})}$$

where D denotes dipolar coupling.

EPR experiments, data processing and restraint determination. DEER traces were collected at Q-band frequencies (~34.4 GHz) and a temperature of 50 K (ref. 50). A commercial X/Q-band Elexsys E580 spectrometer power-upgraded to 200 W and equipped with the homebuilt TE102 rectangular resonator[51] was used. The solution contained the NMR buffer and an rdHDL concentration of approximately 25–35 μM. 10–15 vol.% of deuterated glycerol was added as a cryoprotectant. The samples were placed into quartz tubes, shock-frozen by immersion into liquid nitrogen and inserted into the precooled probe head. All pulses were 12 ns long, the pump frequency was set at the global maximum of the nitroxide EPR spectrum, and the observer frequency was set 100 MHz lower. The DEER traces were processed using the open-source DeerAnalysis package[52], available at http://www.epr.ethz.ch/software.html.

Structure calculation. We used CYANA 3.96 according to a standard protocol[53] for all structure calculations. We used 2 × 205 RDC-derived bond-orientation restraints, 2 × 1,022 PRE-derived upper and lower distance restraints, 2 × 428 NOE-derived upper limit distance restraints, and 6 EPR-derived lower and upper distance restraints. 2 × 284 dihedral angle constraints (Φ and Ψ) from secondary chemical shift analysis were derived from TALOS-N[47]. In addition, symmetry restraints were included on the basis of observation of one single peak per residue in all the NMR spectra. In all, 100 structures were calculated, and the ten conformers that fulfilled the input data best (i.e., those with the lowest CYANA target function) were selected (Ramachandran statistics: 99.8% in the most favored region and 0.2% in additionally allowed region). We considered long-range EPR distance restraints between spin labels in the CYANA calculations by using an approach similar in spirit to that recently used to determine the structure of a protein–RNA complex[54]. For each restraint, the lower and the upper bounds corresponding to the label-to-label distance were derived from the experimental DEER distance distributions. The distance distributions obtained by Tikhonov regularization were not directly used because of the uncertainty in their shape, particularly in the range above 50 Å. In the first CYANA pass, the EPR distance restraints were incorporated as C^β-C^β distances between the labeled residues. We then subjected a representative conformer from the preliminary structure ensemble to rotamer analysis with the open-source package MMM[55] using the R1A_298K_xray rotamer library[56]. For each labeling site, the center of the rotamer cloud was calculated as the population-weighted mean coordinate of the N-O midpoint of the nitroxide moiety of all spin label rotamers. In the second CYANA pass, distances between the center of the rotamer cloud and the backbone N, C′, O and C^α atoms of the labeled residue were used to restrain

a dummy atom (defined as C^{α} of an auxiliary glycine residue) to the center of the rotamer cloud. The experimental mean distance in each pair of spin-labeled sites could thus be treated as the distance between the corresponding dummy atoms, whose position with respect to the backbone was tightly fixed with narrow upper and lower bounds. The structure ensemble was subject to post-computational validation. The rotamer analysis with the R1A_298K_xray rotamer library was performed for all mutation positions for the best ten structures of the final ensemble. The rotamer distributions obtained were used to compute interspin distances and predict the primary DEER signals between the corresponding sites. Figures were prepared using PyMol (Schrödinger). Salt bridges were checked using CoilCheck+ (http://caps.ncbs.res.in/coilcheckplus/action/coilcheckplus-form.php), and cation-π interactions were checked using the CaPTURE server (http://capture.caltech.edu/)[57]. The 3D structure has no intermolecular contacts shorter than 4 Å that show no cross-peak in the NOESY spectra.

Negative-stain TEM and image processing. rdHDL samples were applied to a glow-discharged thin carbon film covering a 200-mesh copper electron microscopy grid and adsorbed for 1 min. Each grid was blotted, washed with three drops of water and negatively stained with two drops of 2% uranyl acetate. The grids were imaged in a Philips CM10 microscope operated at a voltage of 80 kV. Micrographs were recorded with a CCD (charge-coupled device) camera (Veleta, Olympus) over a defocus range of 300–500 nm and with a pixel size of 3.7 Å. In total 42,000 rdHDL particles were selected from 100 micrographs and windowed into 50 × 50–pixel boxes using the BOXER/EMAN 2.1 software[58]. Image processing was performed in RELION[59]. Particle images were corrected for the contrast transfer function (CTFFIND3), normalized and classified to give 2D classes containing approximately 400 images.

Data availability. The assignments for MSPΔH5 have been deposited in the Biological Magnetic Resonance Data Bank under accession number 25710. The rdHDL structure has been deposited in the Protein Data Bank under accession code 2N5E.

44. Marley, J., Lu, M. & Bracken, C. A method for efficient isotopic labeling of recombinant proteins. *J. Biomol. NMR* **20**, 71–75 (2001).
45. Gans, P. *et al.* Stereospecific isotopic labeling of methyl groups for NMR spectroscopic studies of high-molecular-weight proteins. *Angew. Chem. Int. Ed. Engl.* **49**, 1958–1962 (2010).
46. Lee, D., Hilty, C., Wider, G. & Wüthrich, K. Effective rotational correlation times of proteins from NMR relaxation interference. *J. Magn. Reson.* **178**, 72–76 (2006).
47. Shen, Y. & Bax, A. Protein backbone and sidechain torsion angles predicted from NMR chemical shifts using artificial neural networks. *J. Biomol. NMR* **56**, 227–241 (2013).
48. Battiste, J.L. & Wagner, G. Utilization of site-directed spin labeling and high-resolution heteronuclear nuclear magnetic resonance for global fold determination of large proteins with limited nuclear overhauser effect data. *Biochemistry* **39**, 5355–5365 (2000).
49. Permi, P., Rosevear, P.R. & Annila, A. A set of HNCO-based experiments for measurement of residual dipolar couplings in 15N,13C,(2H)-labeled proteins. *J. Biomol. NMR* **17**, 43–54 (2000).
50. Pannier, M., Veit, S., Godt, A., Jeschke, G. & Spiess, H.W. Dead-time free measurement of dipole-dipole interactions between electron spins. 2000. *J. Magn. Reson.* **213**, 316–325 (2011).
51. Polyhach, Y. *et al.* High sensitivity and versatility of the DEER experiment on nitroxide radical pairs at Q-band frequencies. *Phys. Chem. Chem. Phys.* **14**, 10762–10773 (2012).
52. Jeschke, G. *et al.* DeerAnalysis2006—a comprehensive software package for analyzing pulsed ELDOR data. *Appl. Magn. Reson.* **30**, 473–498 (2006).
53. Güntert, P. Automated NMR structure calculation with CYANA. *Methods Mol. Biol.* **278**, 353–378 (2004).
54. Duss, O., Yulikov, M., Jeschke, G. & Allain, F.H. EPR-aided approach for solution structure determination of large RNAs or protein-RNA complexes. *Nat. Commun.* **5**, 3669 (2014).
55. Polyhach, Y., Bordignon, E. & Jeschke, G. Rotamer libraries of spin labelled cysteines for protein studies. *Phys. Chem. Chem. Phys.* **13**, 2356–2366 (2011).
56. Jeschke, G. Conformational dynamics and distribution of nitroxide spin labels. *Prog. Nucl. Magn. Reson. Spectrosc.* **72**, 42–60 (2013).
57. Gallivan, J.P. & Dougherty, D.A. Cation-π interactions in structural biology. *Proc. Natl. Acad. Sci. USA* **96**, 9459–9464 (1999).
58. Tang, G. *et al.* EMAN2: an extensible image processing suite for electron microscopy. *J. Struct. Biol.* **157**, 38–46 (2007).
59. Scheres, S.H. RELION: implementation of a Bayesian approach to cryo-EM structure determination. *J. Struct. Biol.* **180**, 519–530 (2012).